Three-dimensional chiral magnetization structures in FeGe nanospheres

Swapneel Amit Pathak and Riccardo Hertel [*]

Université de Strasbourg, CNRS, Institut de Physique et Chimie des Matériaux de Strasbourg,
UMR 7504, F-67000 Strasbourg, France

Skyrmions, spin spirals, and other chiral magnetization structures developing in materials with an intrinsic Dzyaloshinskii-Moriya interaction display unique properties that have been the subject of intense research in thin-film geometries. Here, we study the formation of three-dimensional chiral magnetization structures in FeGe nanospheres by means of micromagnetic finite-element simulations. In spite of the deep submicron particle size, we find a surprisingly large number of distinct equilibrium states, namely, helical, meron, skyrmion, chiral-bobber, and quasisaturation states. The distribution of these states is summarized in a phase diagram displaying the ground state as a function of the external field and particle radius. This unusual multiplicity of possible magnetization states in individual nanoparticles could be a useful feature for multistate memory devices. We also show that the magnetodipolar interaction is almost negligible in these systems, which suggests that the particles could be arranged at high density without experiencing unwanted coupling.

I. INTRODUCTION

Three-dimensional (3D) nanoscale magnetization structures have recently evolved into a very active field of research [1–3], including, e.g., magnetic structures in complex nanoarchitectures [4], and the tomographic reconstruction of 3D magnetic vector fields in nanocylinders [5]. Various 3D magnetic structures have also been studied in the context of noncentrosymmetric materials, where new configurations such as skyrmion tubes and chiral bobbers have been found [6,7]. In such helimagnetic materials, however, the impact of 3D nanoscale confinement and finite-size effects on the magnetization states has not yet been investigated in detail. It is known that helical states and hexagonal skyrmion lattices can develop in two-dimensional, extended thin films [8,9], and that the additional degree of freedom that is present in thicker films can give rise to further modulations and complex magnetization configurations such as Bloch point structures and chiral bobbers [6,7,10,11]. Moreover, patterned thin-film elements can host a variety of complex chiral structures [12], including isolated skyrmions [13], spin spirals, and "horseshoe"-type structures [14]. Previous studies on finite-size effects in skyrmionic magnetic materials have addressed the impact of the film thickness or the lateral size of thin-film elements, but were generally restricted to flat geometries. To study the influence of nanoscale 3D confinement on the magnetization states forming in a helimagnetic material, we perform finite-element micromagnetic simulations on FeGe nanospheres. In spite of the simplicity of the geometrical shape, we find highly complex magnetic structures in such nanospheres, depending on the particle size and the applied field. This complexity results from the inherently chiral magnetic properties of the noncentrosymmetric material and the constraints imposed by the finite size of the sample.

The general problem addressed in this study, i.e., identifying the size dependence of the magnetic ground state in a nanoparticle, has a long tradition in micromagnetic theory and simulations [15–18]. The question of how a magnetic structure is affected by the particle size is often related to the concept of the single-domain limit [19–25], i.e., the critical size below which the magnetization in a particle remains homogeneous. This, in turn, is connected to the concept of micromagnetic exchange lengths [26,27], which provide material-specific estimates of the characteristic size of fundamental magnetic structures, such as the width of domain walls or the size of vortex cores. The exchange lengths result from competing interactions in micromagnetics. More specifically, they describe a balance between the tendency of the ferromagnetic exchange to maintain a homogeneous magnetic state and other energy terms that favor the formation of inhomogeneous structures. In the case of noncentrosymmetric magnetic materials with intrinsic chiral properties, the long-range helical period $l_d = 4\pi A/|D|$ [28] appears as a further characteristic length. It represents the period of magnetization spirals forming as a compromise between the ferromagnetic exchange and the antisymmetric exchange due to the Dzyaloshinskii-Moriya interaction (DMI). The constant D denotes the strength of the DMI, i.e., the tendency to form helical structures, and A is the ferromagnetic exchange constant. The functional form of l_d is different from that of the magnetostatic exchange length $l_s = \sqrt{2A/\mu_0 M_s^2}$ (M_s is the saturation magnetization and μ_0 is the vacuum permeability), because the former refers to a periodic modulation of the magnetization while the latter describes the width of a localized kink-type transition between two domains. Nevertheless, the long-range helical period l_d can be expected to have similar implications on the size dependence of magnetic structures as the other exchange lengths, namely, that chiral and skyrmionic structures develop in particles with sizes exceeding l_d by a sufficiently large amount.

---
*riccardo.hertel@ipcms.unistra.fr

104414-1

II. MODEL SYSTEM AND NUMERICAL METHOD

We consider spherically shaped nanoparticles of FeGe with a particle radius between 40 and 100 nm, thereby extending previous studies on the formation of magnetic structures in this material in the case of planar geometries [12,29]. The spherical shape serves as a simple, fundamental 3D geometry that can host different magnetization states. Its rounded surfaces are particularly suitable for the formation of swirling magnetization structures that typically develop in helimagnetic materials. With the magnetic structure unaffected by edges and corners [30–32], ellipsoids and spheres traditionally play a fundamental role in determining the size dependence of magnetic structures [33]. FeGe is a well-known B20-type noncentrosymmetric ferromagnet with an intrinsic (bulk) Dzyaloshinskii-Moriya interaction (DMI) [9,13,34–38]. The competition between the symmetric ferromagnetic exchange interaction and antisymmetric DMI gives rise to various complex chiral magnetization configurations. We use our custom-developed general-purpose 3D finite-element micromagnetic software package [39] to investigate the equilibrium magnetization states forming in the presence of such competing interactions within a confined three-dimensional space.

To model the material properties of FeGe, we use $M_s = 384 \, \text{kA m}^{-1}$, $A = 8.78 \times 10^{-12} \, \text{J m}^{-1}$, and $D = 1.58 \times 10^{-3} \, \text{J m}^{-2}$ [12,40]. These material parameters yield a long-range helical period [41] of $l_d = 4\pi A/|D| \simeq 70 \, \text{nm}$ and a magnetostatic exchange length of $l_{\text{ex}} = \sqrt{2A/\mu_0 M_s^2} \approx 9.7 \, \text{nm}$.

The micromagnetic model includes exchange, magnetostatic interaction, DMI, and Zeeman energy. We assume that the material of the nanospheres is isotropic, and hence neglect the contribution of magnetocrystalline anisotropy. The total energy thus reads

$$E = \int \left[A \sum_{i=x,y,z} (\nabla m_i)^2 - \frac{\mu_0}{2} M_s (\boldsymbol{H}_d \cdot \boldsymbol{m}) \right.$$
$$\left. + D\boldsymbol{m} \cdot (\nabla \times \boldsymbol{m}) - \mu_0 M_s (\boldsymbol{H}_{\text{ext}} \cdot \boldsymbol{m}) \right] dV, \quad (1)$$

where $\boldsymbol{m}(\boldsymbol{x}) = \boldsymbol{M}(\boldsymbol{x})/M_s$ is the unit magnetization vector, H_{ext} represents the externally applied field, and $\boldsymbol{H}_d = -\nabla u$ is the magnetostatic field, defined as the gradient field of the magnetostatic scalar potential u [39]. The effective field $\boldsymbol{H}_{\text{eff}}$ is proportional to the variational derivative of the micromagnetic energy with respect to the magnetization, $\mu_0 \boldsymbol{H}_{\text{eff}}(\boldsymbol{r}, t) = -M_s^{-1} \cdot \delta E[\boldsymbol{m}(\boldsymbol{r}, t)]/\delta \boldsymbol{m}$. This effective field is used in the Landau-Lifshitz-Gilbert (LLG) equation [42,43] to calculate the magnetization dynamics.

To numerically determine equilibrium states of the magnetization we perform simulations starting from a random initial configuration of the magnetization $\boldsymbol{M}(\boldsymbol{x})$ and integrate the LLG equation in time until a stable, converged state is found. Several runs are performed with different random initial configurations in order to ascertain that the result represents the ground state, and not a metastable state. Our finite-element software computes the partial effective fields of all energy contributions at each time step and performs

the time integration of the LLG equation using an adaptive Dormand-Prince scheme [44]. Since we are only interested in the static ground state, we choose a high damping constant in the LLG equation ($\alpha = 0.5$) in order to accelerate the calculation and neglect any dynamic process occurring during the relaxation. The time integration of the LLG equation is thus only used as a means to reach a minimum energy state. The magnetostatic field is calculated with a hybrid finite-element method–boundary-element method (FEM-BEM) algorithm that uses $\mathcal{H}^2$ hierarchical matrices [39], allowing for a particularly fast and memory-efficient computation. The spatial discretization is done using irregular tetrahedral meshes [45] with cell sizes not exceeding 2 nm, which is well below the exchange length of the material. A typical mesh used in our simulations contains approximately 6×10^5 elements for a sphere of radius 70 nm.

III. MAGNETIC EQUILIBRIUM STATES

By varying the radius of the nanospheres and the external magnetic field (applied along the positive z direction) we obtain, for each combination of radius and external field, a minimum energy equilibrium magnetization state. We first describe in detail the different types of states that we observe. Afterwards, in Sec. IV, we discuss their distribution as a function of the external field and the particle size. Although, generally speaking, the modifications that the lowest-energy magnetic structures undergo by changing the size and the external field are not continuous, it is to some extent possible to interpret the appearance of different magnetization states as a gradual evolution that is driven by changes in the parameters. To describe such an evolution, we discuss the appearance of different magnetic ground states upon increasing the external magnetic field.

A. Helical state

The helical state is characterized by a continuous rotation of the magnetization along an axis that is nearly perpendicular to the applied field direction. According to our simulations, the helical state is energetically favorable at low external magnetic fields, where the exchange energy and DMI dominate. The magnetization helix is the direct outcome of the competition between the symmetric ferromagnetic exchange interaction and the antisymmetric DMI. This arrangement of the magnetization can also be interpreted as a periodic sequence of narrow alternating domains, pointing along and opposite to the direction of the external magnetic field, and separated by Bloch walls with the same sense of rotation. These alternating domains can be visualized with the help of isosurfaces corresponding to $m_z = 0$, as shown in Fig. 1. In this picture, the $m_z = 0$ isosurfaces can be regarded as *hypothetical* domain walls separating domains aligned parallel and antiparallel to the external field. Since the spatial rotation of the magnetization is rather continuous than localized within domain walls, this interpretation of alternating domains is not strictly correct in micromagnetic terms. Nevertheless, this picture can help to understand the transition towards other states, as will be described later.
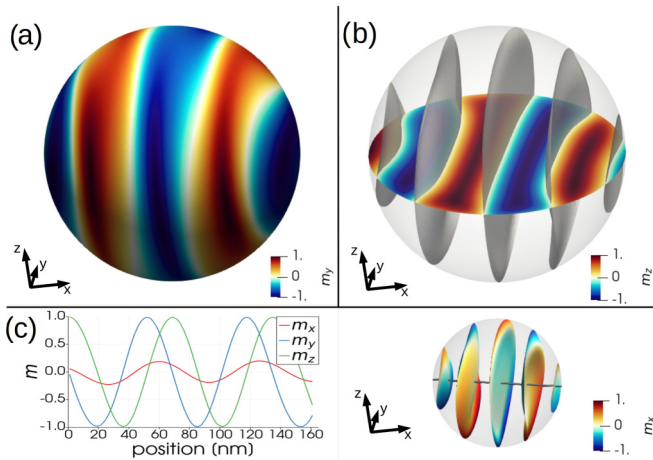
FIG. 1. Helical state in an $r = 80$ nm FeGe sphere at $\mu_0 H_{ext} = 10$ mT. (a) shows the characteristic, regularly alternating contrast in the m_y component on the surface. The external field is applied along the z axis. The gray isosurfaces in (b) display the areas where m_z is equal to zero, while the color code on the central plane illustrates the alternating z component. The magnetization components along the central helix axis are shown in the graph on the left-hand side of (c). The spin spiral is almost perfectly periodic, with a wavelength close to the analytic value of the long-range helical period of the material. The central axis of the helix (right) is slightly tilted, oriented perpendicular to the $m_z = 0$ isosurfaces.

Figure 1 shows a right-handed helix extending throughout the sphere, along an axis that is nominally perpendicular to the external field. The axis of the helix, oriented perpendicular to the $m_z = 0$ isosurfaces, is slightly tilted with respect to the x axis, as shown in Fig. 1(c). One full rotation of the helix (peak-to-peak spacing) occurs on a distance of about 66 nm, which corresponds very well to the analytic value of the long-range helical period [41] of the material $l_d \simeq 70$ nm. The line scan displayed in Fig. 1(c) shows that the computed data fit well with the assumption of a spin spiral with sinusoidal oscillations of the m_z and m_y components along the spiral axis. Minor deviations from the ideal value are expected because the analytic calculation of the spin spiral does not consider problem-specific aspects that are included in the simulation, such as the spherical shape, boundary conditions [46], and the magnetostatic interaction. The small-amplitude oscillations in the m_x component arise from the misalignment of the helix axis and the x axis.

B. Meron state

Interpreting the helical state as a magnetic structure with narrow, alternating domains is helpful in order to understand the evolution of the structure as the applied field is increased. Magnetic domain structures react to an increase of the external field such that the domains oriented parallel to the field grow in size, at the expense of domains oriented antiparallel to it. The transition from a helical state to a meron state (Fig. 2) with increasing external field strength can be interpreted in this sense. The increase of favorably oriented regions is recognizable in the isosurface representation, as the previously almost parallel isosurfaces $m_z = 0$ bend inwards and connect on one side [cf. Figs. 4(d) and 4(e)].
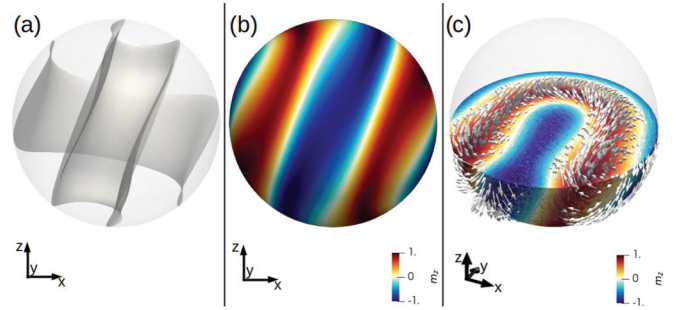
FIG. 2. Three-dimensional meron structure forming in an $r = 70$ nm FeGe nanosphere at $\mu_0 H_{ext} = 30$ mT. The $m_z = 0$ isosurfaces are displayed in (a). When compared with the almost planar isosurfaces of the helical state [cf. Fig. 1(b)], a distinct curvature can be noticed in the meron state. On the sphere surface, the alternating contrast of the z component shows a helical structure similar to the one displayed in Fig. 1(a). The magnetization configuration on a central cross section (c) evidences the 3D meron structure. The state can be interpreted as a combination of a half-helical and half-skyrmion state (cf. Fig. 3).

The simulations yield an augmentation of the tilting of the $m_z = 0$ isosurfaces with respect to the external field direction [Fig. 2(a)] that was already observed in the axis of the helical state [Fig. 1(c)]. Besides the system's general tendency to introduce, to some extent, a spiraling magnetization also along the z direction, we currently do not have a simple explanation for this tilting of the isosurfaces with respect to the external field direction, which we have consistently observed at different size and field parameters.

The field-induced modification of the ground state structure from a helical state to a meron structure is consistent with a decrease of the Zeeman energy while allowing the magnetic system to preserve to a large extent a spiraling magnetic structure on the length scale l_d, as favored by the competition between ferromagnetic exchange and DMI. Note that without DMI, in ordinary ferromagnets, a gradual
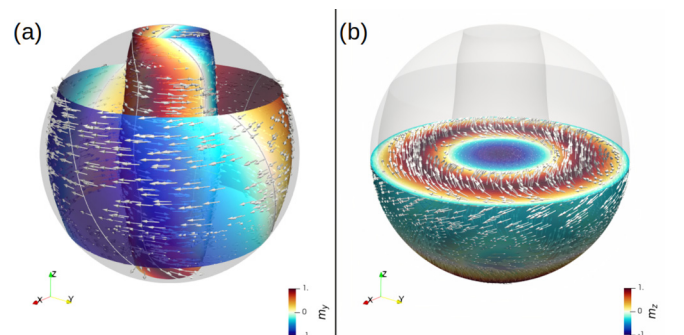
FIG. 3. A 3D skyrmion is the magnetic ground state of an $r = 80$ nm FeGe nanosphere in a 110-mT field. (a) displays the $m_z = 0$ isosurfaces, yielding a skyrmion tube in the center. A second, coaxial tube with opposite swirling is formed at a larger distance. The nonuniform distribution of the m_y component on the tubes shows that both $m_z = 0$ isosurfaces are twisted along the z direction. The magnetic configuration on a horizontal slice in the middle is shown in (b), displaying strong similarities with the well-known magnetization texture of a two-dimensional Bloch skyrmion in thin films.
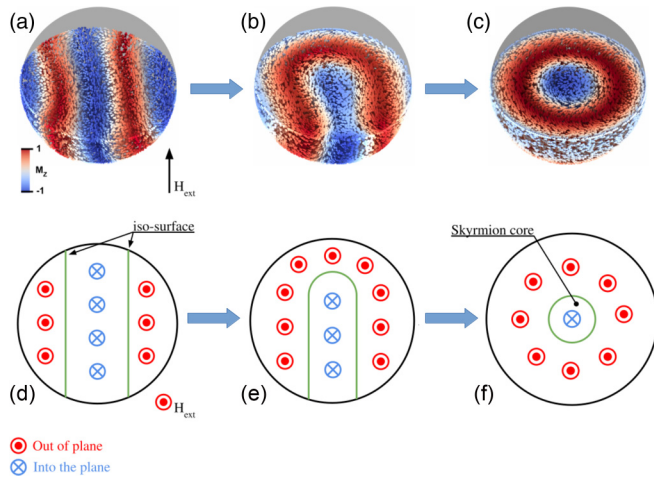
FIG. 4. Transformation of the magnetic ground state from a helical state (left) into a meron state (middle) towards a skyrmion state (right) as the external field increases. The top row (a)–(c) displays simulation results, where the top hemisphere is removed to show the magnetic structure on the central plane. The thick arrows between the frames indicate an increase of the external field. The color code, from blue to red, denotes the magnetization component m_z antiparallel and parallel to the field direction, respectively. In the bottom row, the schematics (d)–(f) of the top view show, in a simplified way, the evolution of equilibrium states as the field is increased. The growth of the domains pointing in the direction of the field is not achieved by reducing the width of the central domain, but by connecting the isosurfaces, yielding first the meron state and, at higher fields, the skyrmion state.

modification of a periodic domain structure in an increasing external field would occur in a different way, namely by reducing or increasing the distance between neighboring domain walls. Such a domain wall displacement, however, would have a detrimental effect on the periodicity of the spin spirals, and is thus not a viable channel in chiral magnetic materials.

An alternative interpretation of the meron structure consists in considering the magnetization state as a hybrid form of two different chiral structures. To illustrate this, the description on the magnetization state can be split in two parts, separated by the central $y = 0$ plane. The part of the nanosphere on the front of Fig. 2(c) appears to preserve the structure of a helical state, while the part on the rear displays the characteristic concentric domains of a skyrmion, which will be discussed in the following section. In this sense, the meron state can be considered as an intermediate, transitional structure between these two states. Meron structures are known from extended two-dimensional system. In such thin films, theory predicts that merons are unstable in isolation, and that instead bimeron states should form [47]. However, here, the finite sample size represents a stabilizing factor. We also note that similar examples of isolated meron states have been reported in rectangular shapes [47] and in disk geometries [14,48], where the structure was denoted as a "horseshoe" state, for obvious reasons.

C. Skyrmion state

Further increasing the external field strengthens the tendency to expand the regions—or domains—in which the

magnetization is aligned along the field direction. This tendency is balanced by the necessity to preserve spin spirals, as required by the interplay of symmetric and antisymmetric exchange. In the isosurface representation, the evolution of a meron state in an increasing external field can be interpreted as a second inwards bending of the isosurfaces, now connecting the isosurfaces on the opposite side, thereby yielding a circular central core in which the magnetization points opposite to the applied field [Figs. 4(e) and 4(f)]. The resulting axially symmetric configuration is the skyrmion state.

The isosurface representation allows us to visualize the concentric shape of the magnetization structure of the skyrmion. The inner $m_z = 0$ isosurface separates the skyrmion core from the bulk [Fig. 3(a)]. This central cylindrical region is sometimes referred to as a *skyrmion tube* or skyrmion line, and it has recently been discussed in the context of high-frequency modes [49]. In addition to the $m_z = 0$ isosurface around the core region, a further cylindrical isosurface appears at a larger distance from the central axis, indicating a second zero crossing of the m_z component. This is consistent with the formation of helical structures imposed by the DMI, which now form in a radial direction and with cylindrical wave fronts. The outer cylindrical isosurface of the skyrmion state can also be interpreted as the result of a connection of the "horseshoe"-shaped outer isosurface of the meron state, shown in Fig. 2(a).

The main features of the skyrmion structure are readily recognized by displaying the magnetic configuration on a horizontal slice on the central plane, as shown in Fig. 3(b). The magnetization configuration on the central slice exhibits obvious similarities with the well-known magnetization texture of a two-dimensional Bloch skyrmion in a thin film. However, the 3D structure in the sphere has additional features. For instance, the magnetic structure undergoes a twist along the axial direction, as shown in Fig. 3(a), to reduce the DMI energy in the nanosphere. A similar behavior was previously reported by Rybakov *et al.* [10] in the case of thick extended films.

D. Chiral-bobber state

If the external field is further increased, the central core of the skyrmion state pointing in the opposite direction of the field shrinks in size, and the surrounding circular domain oriented along the external field grows. At a certain field, the axially symmetric skyrmion state becomes unstable and transforms into a different magnetization configuration, known as chiral-bobber state [6]. This structure retains to some extent the central skyrmion core, which now however terminates in a Bloch point structure [50,51] inside the sphere [cf. Figs. 5(d) and 5(e)]. The chiral-bobber state can thus be regarded as a hybrid state combining the skyrmion and Bloch point structure. The complicated magnetic structure of the chiral-bobber state in a nanosphere is illustrated in Fig. 6. There, the purple dot at the apex of the bobber-shaped isosurface indicates the position of the Bloch point [52,53].

To further analyze this magnetic configuration, we display in Fig. 7 the magnetic structure on two horizontal slices, one above and one below the Bloch point. The configuration on the upper slice resembles that of a skyrmion state, while the one
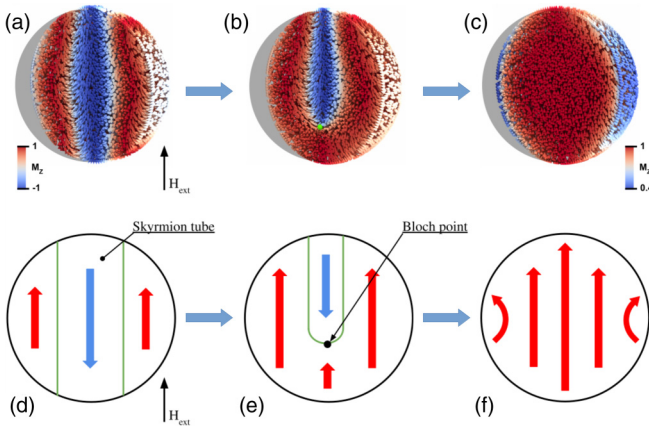
FIG. 5. With increasing field, the skyrmion state (left) transforms first into the chiral-bobber state (middle), which then further evolves into a quasisaturation state (right). In the simulated structures (a)–(c) half of the sphere has been removed to display the evolution and disappearance of the skyrmion tube in the center of the sample. The red and blue color code refers to the value of the magnetization component m_z parallel and antiparallel to the field, respectively. The schematics in the bottom row (d)–(f) illustrate how the skyrmion core, representing a nanodomain aligned opposite to the field, shrinks as the external field increases. This central domain first becomes smaller as a Bloch point is injected, yielding the chiral-bobber state, then it vanishes completely, resulting in a quasisaturation state with a DMI-induced twist on the surface.

below corresponds to a nearly homogeneous configuration in which the magnetization is largely aligned in the direction of the external field. The line scans in Fig. 7(b) display the hugely different evolution of the magnetization along the radius of these two slices. While the skyrmionlike structure in the central plane evidences strong variations in the axial component m_z as well as in the azimuthal component m_φ,
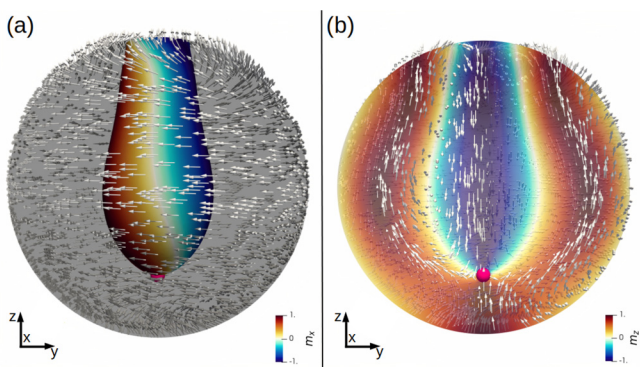
FIG. 6. The chiral-bobber state shown here at $\mu_0 H_{\text{ext}} = 200\,\text{mT}$ and at $r = 80\,\text{nm}$, is a complex 3D magnetization structure in which a skyrmion tube terminates in a Bloch point. In (a), the characteristic cone shape of the residual skyrmion core is visualized by the $m_z = 0$ isosurface, color coded by the value of the x component of the magnetization circulating around the central axis. (b) shows the same structure on a vertical cross section. Here, the color code refers to the z component of the magnetization. The purple sphere denotes the position of the Bloch point, defined as a point in which the m_x, m_y, and m_z components are zero.
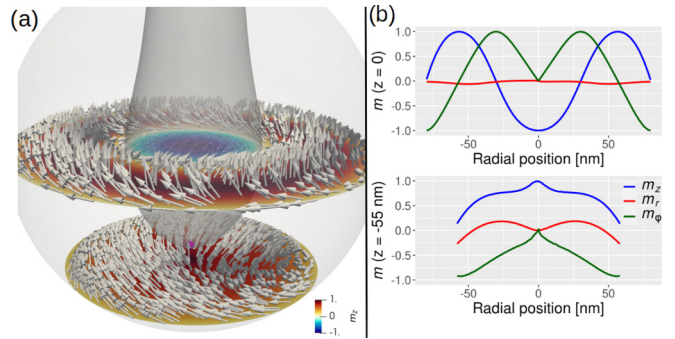
FIG. 7. (a) shows an alternative representation of the magnetization configuration of Fig. 6. It displays the magnetization on two slices, one above (at $z = 0$) and one below the Bloch point (at $z = -55\,\text{nm}$). On the slice above the Bloch point the structure is similar to the skyrmion state, while below the Bloch point the magnetization is almost saturated along the field direction. The top and bottom graphs in (b) display the axial (blue, m_z), radial (red, m_r), and azimuthal (m_φ) components of the magnetization on a radial line on the center and bottom slice, respectively.

the magnetization is largely magnetized uniformly along the z direction on the lower slice, showing only a more pronounced azimuthal twist at the perimeter.

Chiral-bobber structures have been previously reported, both in theoretical [6] and experimental [54] studies, in thick extended films of noncentrosymmetric ferromagnets. Recently, this magnetization structure has attracted considerable attention as it has been proposed as a candidate for a fundamental unit of information storage, along with the skyrmion state, in future spintronics memory devices [54].

If the external field is further increased, the central core of the chiral-bobber state shrinks in a lateral direction until, at a certain field, the Zeeman energy dominates and a quasisaturated state becomes energetically favorable, as illustrated in Figs. 5(e) and 5(f).

E. Saturation state

At large external fields, a relatively simple equilibrium state develops, which is characterized by the bulk of the magnetization pointing along the external magnetic field direction as shown in Fig. 8. This configuration resembles an ordinary ferromagnetic saturation state. However, near the surface the magnetization deviates, in particular along the equatorial plane. This deviation is primarily due to the DMI, which tends to preserve a chiral structure as far as possible in the presence of a strong external field. The slight curling of the magnetization induced by the DMI is also favored by magnetostatics, because the system thereby reduces the magnetostatic surface charges as it forms a weakly developed vortex state. Furthermore, the particle surface plays a particular role in the curling of the magnetization due to specific boundary conditions of the DMI interaction [46].

IV. PHASE DIAGRAM

In the previous section, we have identified five principal equilibrium states of the chiral magnetization in a FeGe
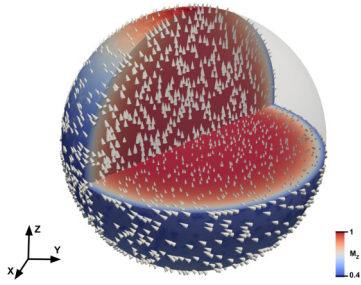
FIG. 8. Quasisaturated magnetization state in an $r = 80$ nm FeGe sphere at $\mu_0 H_{ext} = 500$ mT. At such high external magnetic fields, the tendency to minimize the Zeeman energy dominates and the bulk of the magnetization is aligned in the direction of the field. However, a rather significant deviation, which is primarily due to the DMI, occurs at the boundary near the equatorial plane.

nanosphere, and described their evolution with increasing external field. The stability of these structures, however, also depends on the particle size. To investigate these dependencies, we have performed numerous additional simulations. The numerical results allow us to determine the stability ranges of the five states, as summarized in the phase diagram shown in Fig. 9. The diagram displays the lowest-energy configuration as a function of the external magnetic field and the radius of the nanospheres.

Remarkably, the skyrmion phase does not exist as a ground state in FeGe nanospheres below a radius of 65 nm, and it becomes unstable below about 55 nm. Given that the long-range helical period of the material is l_d (70 nm), this result indicates that the size of the sphere should be large enough to accommodate almost two full rotations of the magnetization across the diameter in order to host a 3D skyrmion structure. This trend of disappearing phases continues as we further decrease the radius. Below the radius of 50 nm, as the nanosphere diameter approaches l_d, the chiral-bobber and meron phase also cease to be ground states. At this size, only the helical phase (at lower external fields) and the saturation phase (at higher external fields) are lowest-energy states. For
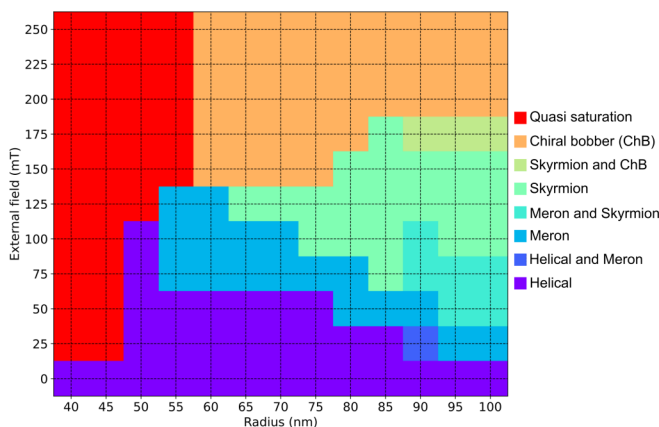
radii smaller than 40 nm, only the saturation phase remains as the particle size falls below l_d, leaving no room for even one full rotation of the magnetization.

A clear distinction of the five principal configurations mentioned above is only possible in particle sizes up to a radius of about 90 nm. In larger nanospheres, hybrid structures appear, which can contain, e.g., both a meron and skyrmion structure, or a skyrmion as well as a chiral bobber. At these larger sizes, the impact of the particle's spherical shape on the magnetic structure diminishes, and one observes a gradual transition towards a quasicontinuum of 3D chiral magnetization states, as it would occur in bulk material.

A. Impact of magnetostatic interaction

Having described the various magnetic structures and their formation resulting from the competing interactions of Zeeman energy, ferromagnetic exchange, and DMI, we now discuss the impact of the dipolar (magnetostatic) field on these configurations and their distribution. To illustrate the quantitative impact of the dipolar magnetic field, Fig. 10 displays the demagnetization energy as a percentage of the total energy for respective equilibrium states.

It is well known that, in the case of ordinary ferromagnets, the magnetostatic interaction has a decisive impact on the formation of inhomogeneous magnetic structures. The size-dependent equilibrium structure in ordinary ferromagnetic nanoparticles is primarily determined by the balance of the competing interaction of the magnetostatic energy favoring flux-closure states and the ferromagnetic exchange that tends to prevent inhomogeneities of the magnetization. The equilibrium structure is also impacted by the strength of an external magnetic field, and thus the field- and size-dependent distribution of magnetic states in nanoparticles is commonly summarized in phase diagrams similar to ours [15]. However, in our case, the competition is primarily driven, on one side, by the tendency to align the magnetization along the external

FIG. 9. Phase diagram of the magnetic ground state of a FeGe nanosphere as a function of the external magnetic field and the radius. The different regions outline the parameter ranges in which respective magnetization states represent the lowest-energy configuration.
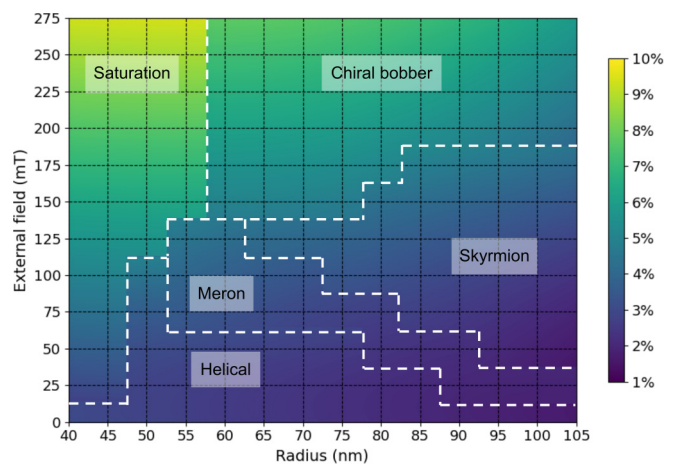
FIG. 10. Demagnetization energy as a percentage of the total energy for different magnetic ground states in the phase diagram. In all cases the maximum value remains below 10% through out the phases. The percentage increases only slightly towards the regions of small radius and high fields, where the nanospheres are in the saturation phase.

field direction and, on the other side, by the material's tendency to develop spiraling magnetization structures on the length scale l_d, which in turn is the result of a balance between the ferromagnetic and the antisymmetric exchange interaction. In this latter case, the role of the demagnetizing field is not clear, and it is in fact often neglected in simulations of chiral magnetization structures.

To analyze the impact of magnetostatic interactions on these configurations and their distribution in the phase diagram, we repeated the calculations by excluding the demagnetization field from the simulation. Remarkably, we found that this does not alter the results appreciably, yielding in fact essentially the same phase diagram (not shown). This is consistent with the observation that the relative impact of the demagnetization energy, displayed in Fig. 10 as the percentage of total energy, is relatively small for all equilibrium states. The demagnetization energy does not exceed 10% of the total energy for any of the states. This indicates that, although not strictly negligible, magnetostatic interactions do not play a dominant role in the equilibrium state configuration and distribution. The overall very low relative value of the demagnetization energy shows in particular that this energy term does not play an important role in the competition of the interactions leading to the complex structures discussed before. In fact, the demagnetization energy becomes only sizable in the upper left part of the plot, i.e., towards small radius sizes and high fields, where the particles are in a quasisaturation state. In the other equilibrium states, the DMI-induced helical nature of the magnetization structures already reduces the magnetostatic energy by forming states similar to periodically alternating domains, or swirling patterns. The balance between ferromagnetic exchange and DMI thus leads to the formation of magnetic structures which provide a fair amount of magnetic flux closure, so that the demagnetizing energy of the DMI-induced structures remains relatively low. Dipolar fields therefore do not have a decisive impact on helical or chiral magnetization structures. In conclusion, our results indicate that neglecting the magnetostatic interaction is a perfectly acceptable approximation in the simulation of magnetic materials with strong DMI, at least in the case of 3D nanoparticles. This is not necessarily true for flat and thin geometries, where demagnetizing fields generally play a larger role, and where the magnetic surface charges generated by chiral structures have a stronger relative impact on the total demagnetizing energy. Moreover, the reduced dimensionality of thin films may lower the degree by which chiral or helical magnetization states can achieve a partial magnetic flux closure.

V. METASTABILITY AND ENERGY VARIATIONS

The phase diagram representation discussed in the previous section describes a cartography of magnetic ground states as a function of size and external field strength. This form of data visualization helps understanding the succession of various lowest-energy configurations upon changes of either the applied field or the particle diameter, but it does not provide quantitative information on the energy of these configurations, nor on how the energy varies within the studied parameter range. Moreover, by singling out the magnetization state with
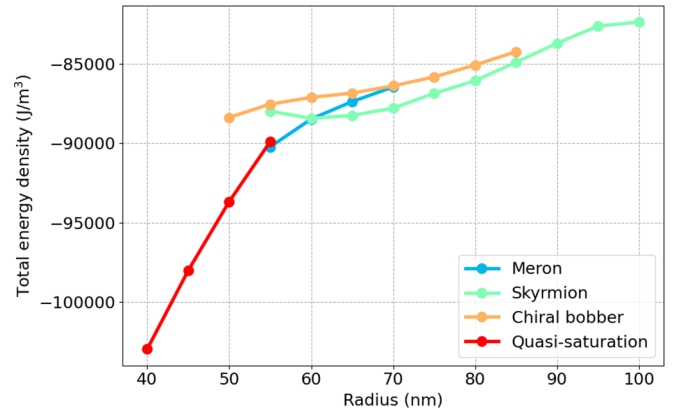
FIG. 11. Average micromagnetic energy density of different magnetic configurations as a function of size, at a constant field value of $\mu_0 H_{ext} = 125\,\mathrm{mT}$. Different magnetization states can be stable over relatively large range of sizes. The phase diagram in Fig. 9 identifies only the lowest-energy configuration.

the lowest energy, it does not reflect the fact that several different configurations can be stable at the same parameter values.

In order to clarify these aspects, Fig. 11 displays the energy of four different magnetic structures as a function of the particle size in the case of fixed external field strength $\mu_0 H_{ext} = 125\,\mathrm{mT}$. The energy is represented as the spatially averaged value of the sum of the energy densities due to the exchange, the DMI, the magnetostatic, and the Zeeman term. This example shows that, at certain sizes and field strengths, the FeGe nanospheres can adopt several different magnetization states. In some cases the relative difference in energy between these configurations can be very small. For instance, at 55 nm radius, the quasisaturated state and the meron configuration yield a very similar value of the total energy, and the total energies of the skyrmion state and the meron state are almost identical at 60 nm radius.

A similar situation can also be observed in Fig. 12, which shows the variation of the energy of different magnetization states as a function of the external field strength. In the vicinity of $\mu_0 H_{ext} = 125\,\mathrm{mT}$, the energies of the meron, skyrmion, and chiral-bobber states fall within a comparatively small range, differing by less than 2%. While energy differences of this magnitude can be resolved in the simulations, there can also be situations in which the energy difference between two different magnetization states is so small as to approach the inevitable limits of numerical accuracy. Although such situations with nearly degenerate states may result in an uncertainty about the precise position of boundaries in the phase diagram, these cases are rare and not of particular importance. These effects only concern details of the overall picture and have a negligible effect on the subdivision into different regions as described in the phase diagram of Fig. 9.

In this context of metastable configurations it should also be noted that, in general, the different magnetization states are separated by large energy barriers. Therefore, two different states can each display strong stability, in spite of having nearly identical energies. Analyzing the barrier height
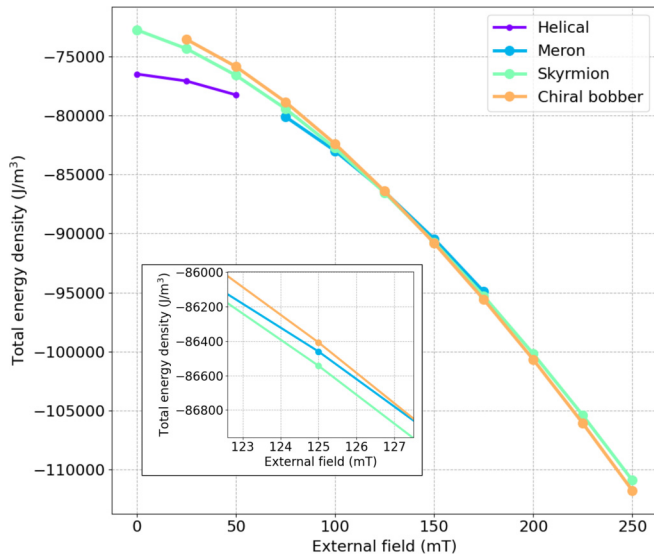
FIG. 12. Average micromagnetic energy densities of various stable and metastable magnetization states as a function of the applied external field strength. The particle radius is constant and equal to $r = 70$ nm. The inset shows a magnified view on the field range around 125 mT, in the vicinity of the intersection points of three curves with similar energies.

between the various states is a nontrivial task [55] that goes beyond the scope of this study.

Finally, as an example to illustrate how the individual energy terms contribute to the total energy of the system, Fig. 13 displays the partial energies of the skyrmion state at 125 mT as a function of the particle radius. As a general tendency, one can notice that the absolute value of all energy density terms decreases with increasing particle size. This is a normal observation in micromagnetics, as an increas-
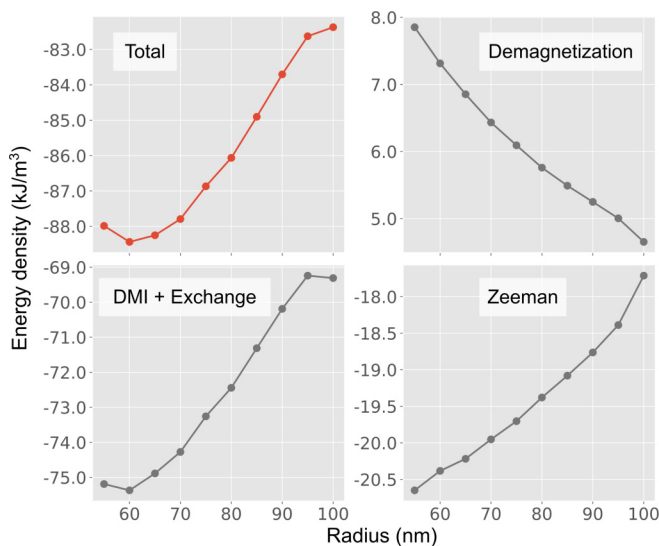
FIG. 13. Variation of the partial energy densities of the skyrmion state as a function of the particle size. The total energy density (red curve in the top left panel) is the sum of the partial energy contributions displayed in the other panels. The external field value is kept fixed at 125 mT.

ing volume generally gives the system more possibilities to adapt the magnetic structure such as to reduce the average energy density. Figure 13 further shows that the total energy is largely dominated by the contributions of the DMI and the ferromagnetic exchange energy. By contrast, the dipolar (demagnetization) energy is about an order of magnitude smaller than the sum of the antisymmetric and symmetric exchange terms, in accordance with the discussion in Sec. IV A. The kink appearing at $r = 95$ nm indicates a qualitative change in the micromagnetic structure. As mentioned before, the finite sample geometry ceases to provide an efficient spatial confinement for individual magnetic structures at sizes larger than $r \simeq 90$ nm. The transition to a quasicontinuum of chiral magnetization occurring at these sizes results in magnetic structures that cannot be uniquely classified into the main states discussed in Sec. III.

VI. CONCLUSION

Using three-dimensional finite-element micromagnetic simulations, we identified a collection of possible magnetization states in FeGe nanospheres and classified them into five principal categories: Helical, meron, skyrmion, chiral-bobber, and saturation states. Each of these states can develop as a stable minimum-energy configuration depending on the particle size and external field. This multitude of well-defined magnetic states largely exceeds the variety of magnetic structures that are known from ordinary ferromagnetic nanoparticles, where the size- and field-dependent variations of the magnetic structure are typically limited to a transition from a homogeneous state to a flux-closure vortex state. In contrast to this, the rich spectrum of magnetic structures in FeGe nanospheres offers the possibility to switch between distinctly different states and thus bears interesting potentials for applications as nanoscale multistate data storage units.

We note that the geometric confinement, provided by the spherical shape of the nanospheres, allows for the formation of the respective states in isolation. The formation of such structures in individual nanoparticles, with a well-defined position and orientation, makes it possible to directly address these magnetic structures, thereby opening a pathway towards further investigations on their individual static and dynamic properties.

Our simulations have further allowed us to analyze the influence of magnetostatic interactions on the formation of the magnetic equilibrium configurations and their distribution within a phase diagram. Unlike ferromagnetic particles, where demagnetizing fields decisively impact the equilibrium states, we find that magnetostatic fields only play a negligible role in the case of chiral magnetic structures in FeGe nanospheres. This suggests that, when simulating 3D structures with strong DMI effects, it is acceptable to omit dipolar fields, whose calculation is usually the most expensive part in numerical terms. From a possible application perspective, the small impact of magnetostatic interactions in these systems indicates that it should be possible to arrange such magnetic nanoparticles close to each other without experiencing an unwanted coupling.

ACKNOWLEDGMENTS

[1] A. Fernández-Pacheco, R. Streubel, O. Fruchart, R. Hertel, P. Fischer, and R. P. Cowburn, Nat. Commun. **8**, 15756 (2017).

[2] P. Fischer, D. Sanz-Hernández, R. Streubel, and A. Fernández-Pacheco, APL Mater. **8**, 010701 (2020).

[3] L. Skoric, D. Sanz-Hernández, F. Meng, C. Donnelly, S. Merino-Aceituno, and A. Fernández-Pacheco, Nano Lett. **20**, 184 (2020).

[4] L. Keller, M. K. I. A. Mamoori, J. Pieper, C. Gspan, I. Stockem, C. Schröder, S. Barth, R. Winkler, H. Plank, M. Pohlit *et al.*, Sci. Rep. **8**, 6160 (2018).

[5] C. Donnelly, M. Guizar-Sicairos, V. Scagnoli, S. Gliga, M. Holler, J. Raabe, and L. J. Heyderman, Nature (London) **547**, 328 (2017).

[6] F. N. Rybakov, A. B. Borisov, S. Blügel, and N. S. Kiselev, Phys. Rev. Lett. **115**, 117201 (2015).

[7] F. N. Rybakov, A. B. Borisov, S. Blügel, and N. S. Kiselev, New J. Phys. **18**, 045002 (2016).

[8] S. Muhlbauer, B. Binz, F. Jonietz, C. Pfleiderer, A. Rosch, A. Neubauer, R. Georgii, and P. Boni, Science **323**, 915 (2009).

[9] X. Z. Yu, N. Kanazawa, Y. Onose, K. Kimoto, W. Z. Zhang, S. Ishiwata, Y. Matsui, and Y. Tokura, Nat. Mater. **10**, 106 (2011).

[10] F. N. Rybakov, A. B. Borisov, and A. N. Bogdanov, Phys. Rev. B **87**, 094424 (2013).

[11] P. Milde, D. Köhler, J. Seidel, L. M. Eng, A. Bauer, A. Chacon, J. Kindervater, S. Mühlbauer, C. Pfleiderer, S. Buhrandt *et al.*, Science **340**, 1076 (2013).

[12] M. Beg, R. Carey, W. Wang, D. Cortés-Ortuño, M. Vousden, M.-A. Bisotti, M. Albert, D. Chernyshenko, O. Hovorka, R. L. Stamps *et al.*, Sci. Rep. **5**, 17137 (2015).

[13] F. Zheng, H. Li, S. Wang, D. Song, C. Jin, W. Wei, A. Kovács, J. Zang, M. Tian, Y. Zhang, H. Du, and R. E. Dunin-Borkowski, Phys. Rev. Lett. **119**, 197205 (2017).

[14] V. Karakas, A. Gokce, A. T. Habiboglu, S. Arpaci, K. Ozbozduman, I. Cinar, C. Yanik, R. Tomasello, S. Tacchi, G. Siracusano *et al.*, Sci. Rep. **8**, 7180 (2018).

[15] W. Rave, K. Fabian, and A. Hubert, J. Magn. Magn. Mater. **190**, 332 (1998).

[16] W. Rave and A. Hubert, IEEE Trans. Magn. **36**, 3886 (2000).

[17] N. A. Usov, C.-R. Chang, and Z.-H. Wei, J. Appl. Phys. **89**, 7591 (2001).

[18] R. Hertel and H. Kronmüller, J. Magn. Magn. Mater. **238**, 185 (2002).

[19] J. Frenkel and J. Doefman, Nature (London) **126**, 274 (1930).

[20] L. Néel, C. R. Acad. Sci. Paris **224**, 1488 (1947).

[21] C. Kittel, Phys. Rev. **70**, 965 (1946).

[22] W. F. Brown, J. Appl. Phys. **39**, 993 (1968).

[23] R. P. Cowburn, D. K. Koltsov, A. O. Adeyeye, M. E. Welland, and D. M. Tricker, Phys. Rev. Lett. **83**, 1042 (1999).

[24] N. A. Usov, L. G. Kurkina, and J. W. Tucker, J. Phys. D **35**, 2081 (2002).

[25] A. Yamasaki, W. Wulfhekel, R. Hertel, S. Suga, and J. Kirschner, Phys. Rev. Lett. **91**, 127201 (2003).

[26] H. Kronmüller, Z. Phys. **168**, 478 (1962).

[27] H. Kronmüller and M. Fähnle, *Micromagnetism and the Microstructure of Ferromagnetic Solids* (Cambridge University Press, Cambridge, U.K., 2003).

[28] H. Wilhelm, M. Baenitz, M. Schmidt, C. Naylor, R. Lortz, U. K. Rößler, A. A. Leonov, and A. N. Bogdanov, J. Phys.: Condens. Matter **24**, 294204 (2012).

[29] X. Zhao, C. Jin, C. Wang, H. Du, J. Zang, M. Tian, R. Che, and Y. Zhang, Proc. Natl. Acad. Sci. USA **113**, 4918 (2016).

[30] W. Rave, K. Ramstöck, and A. Hubert, J. Magn. Magn. Mater. **183**, 329 (1998).

[31] A. Thiaville, D. Tomáš, and J. Miltat, Phys. Status Solidi A **170**, 125 (1998).

[32] A. Hubert, J. Phys. Colloq. **49**, C8-1859 (1988).

[33] C. Kittel, Rev. Mod. Phys. **21**, 541 (1949).

[34] P. Bak and M. H. Jensen, J. Phys. C **13**, L881 (1980).

[35] Y. Ishikawa, K. Tajima, D. Bloch, and M. Roth, Solid State Commun. **19**, 525 (1976).

[36] I. Dzyaloshinsky, J. Phys. Chem. Solids **4**, 241 (1958).

[37] T. Moriya, Phys. Rev. **120**, 91 (1960).

[38] A. N. Bogdanov, U. K. Rößler, M. Wolf, and K.-H. Müller, Phys. Rev. B **66**, 214410 (2002).

[39] R. Hertel, S. Christophersen, and S. Börm, J. Magn. Magn. Mater. **477**, 118 (2019).

[40] D. Cortés-Ortuño, M. Beg, V. Nehruji, L. Breth, R. Pepper, T. Kluyver, Gary Downing, T. Hesjedal, P. Hatton, T. Lancaster *et al.*, New J. Phys. **20**, 113015 (2018).

[41] B. Lebech, J. Bernhard, and T. Freltoft, J. Phys.: Condens. Matter **1**, 6105 (1989).

[42] L. D. Landau and E. Lifshitz, Phys. Z. Sowjet. **8**, 153 (1935).

[43] T. L. Gilbert, IEEE Trans. Magn. **40**, 3443 (2004).

[44] K. Ahnert and M. Mulansky, AIP Conf. Proc. **1389**, 1586 (2011).

[45] C. Geuzaine and J.-F. Remacle, Int. J. Numer. Methods Eng. **79**, 1309 (2009).

[46] S. Rohart and A. Thiaville, Phys. Rev. B **88**, 184422 (2013).

[47] M. Ezawa, Phys. Rev. B **83**, 100408(R) (2011).

[48] G. Hrkac, C.-M. Pfeiler, D. Praetorius, M. Ruggeri, A. Segatti, and B. Stiftner, Adv. Comput. Math. **45**, 1329 (2019).

[49] S.-Z. Lin, J.-X. Zhu, and A. Saxena, Phys. Rev. B **99**, 140408(R) (2019).

[50] O. V. Pylypovskyi, D. D. Sheka, and Y. Gaididei, Phys. Rev. B **85**, 224401 (2012).

[51] C. Andreas, A. Kákay, and R. Hertel, Phys. Rev. B **89**, 134403 (2014).

[52] W. Döring, J. Appl. Phys. **39**, 1006 (1968).

[53] E. Feldtkeller, Z. Angew. Phys. **19**, 530 (1965).

[54] F. Zheng, F. N. Rybakov, A. B. Borisov, D. Song, S. Wang, Z.-A. Li, H. Du, N. S. Kiselev, J. Caron, A. Kovács *et al.*, Nat. Nanotechnol. **13**, 451 (2018).

[55] R. Dittrich, T. Schrefl, D. Suess, W. Scholz, H. Forster, and J. Fidler, J. Magn. Magn. Mater. **250**, 12 (2002).